

Coherent control of solid-state defect spins via patterned boron-doped diamond circuit

Masahiro Ohkuma¹, Eikichi Kimura¹, Ryo Matsumoto^{2,*}, Shumpei Ohyama¹, Saki Tsuchiya¹,
Harim Lim³, Yong Soo Lee³, Junghyun Lee³, Yoshihiko Takano², and Keigo Arai^{1†}

¹*School of Engineering, Institute of Science Tokyo, Yokohama, Kanagawa 226-8501, Japan*

²*Research Center for Materials Nanoarchitectonics (MANA),*

National Institute for Materials Science, Tsukuba, Ibaraki 305-0047, Japan and

³*Center for Quantum Information, Korea Institute of Science and Technology, Seoul, 02792, Republic of Korea*

(Dated: December 23, 2024)

We investigate the electrical transport characteristics of boron-doped diamond (BDD) across frequencies ranging from direct current to 3 GHz to explore the potential of BDD circuits as microwave waveguides. Three homoepitaxial BDD films with varying boron concentrations, exhibiting insulating to metallic properties, are fabricated on a single-crystalline diamond substrate containing nitrogen-vacancy (NV) centers. The Ω -shaped BDD circuit demonstrates an approximately 30 Ω impedance at the resonance frequency of the NV center, facilitating the propagation of microwaves over the circuit, even with a standard 50 Ω reference impedance. We successfully perform optically detected magnetic resonance (ODMR) on NV centers within diamonds using BDD circuits and observed continuous-wave ODMR spectra across all circuits. Additionally, we record Rabi oscillations in pulsed ODMR measurements using the metallic BDD circuit. The integration of NV centers with BDDs presents a compact, robust, and adaptable platform for quantum sensing in challenging environments and for quantum information processing.

I. INTRODUCTION

Diamond is a versatile material capable of accommodating various impurities, which can modify its electronic, thermal, and optical properties. When doped with boron, it can transform into a p-type semiconductor, potentially entering a metallic state and demonstrating superconductivity at low temperatures [1–4]. Boron-doped diamond (BDD) can be synthesized into thin films through microwave plasma chemical vapor deposition, facilitating the creation of superconducting quantum interference devices and microwave devices [5–8]. The BDD thin film enables the transmission of alternating electric currents across a broad frequency spectrum, thereby presenting significant opportunities for its use in electric circuits. These distinctive properties may pave the way for diverse applications in innovative devices, including power electronics [9–11] and quantum technologies [12].

The negatively charged nitrogen-vacancy (NV) center, another type of point defect within the diamond lattice, has emerged as a prominent quantum platform owing to its unique advantages [13–22]. Notably, the NV center allows for coherent control across a wide range of operating conditions, including pressures spanning from ultrahigh vacuum to 130 GPa [23–25] and temperatures ranging from 0.35 to 1400 K [26–29]. Additionally, control systems for the NV center can be miniaturized, integrated, and made portable, facilitating various practical applications [30–33]. These applications necessitate the use of alternating electromagnetic fields, including approximately GHz-scale microwaves for manipulating the ground state

manifolds of electronic spin [34], MHz-scale radio frequency waves for nuclear spin control [35–37], and kHz-scale alternating currents for electronic spin phase modulation [38, 39]. These fields are generated by electrical circuits made from metals like gold and copper, which are often deposited on a thin titanium adhesive layer. However, the use of metal circuits poses challenges, such as susceptibility to scratching and corrosion, and the need for chemical etching to remove the adhesive layer. Transitioning to using BDD in these circuits could significantly improve their durability and simplify the overall system.

In this study, we employ a thin film of Ω -shaped BDD as a source of alternating magnetic fields to coherently manipulate an ensemble of NV centers in diamond. Our principal findings include: (i) the impedance of the BDD thin films is effectively modeled up to 3 GHz using a lumped parameter circuit model, (ii) metallic-state BDD with high boron concentration can generate microwave fields that are on par with those produced by conventional metal wires, and (iii) the generated field exhibits uniformity to within 3% across 25 μm around the center. We foresee that BDD could serve as a flexible solution for controlling NV systems under extreme conditions and for homoepitaxial integration on the same chip, thereby enhancing fabrication convenience and improving thermal dissipation. In the following sections, we provide a detailed account of our experimental results and discuss their implications for potential applications.

II. OVERVIEW OF BDD–NV SYSTEM

The BDD–NV system consists of an Ω -shaped BDD circuit fabricated on a diamond substrate that contains an ensemble of NV centers, as illustrated in Fig. 1. This study examines three variants of BDD, labeled BDD1,

* MATSUMOTO.Ryo@nims.go.jp

† arai.k.835f@m.isct.ac.jp

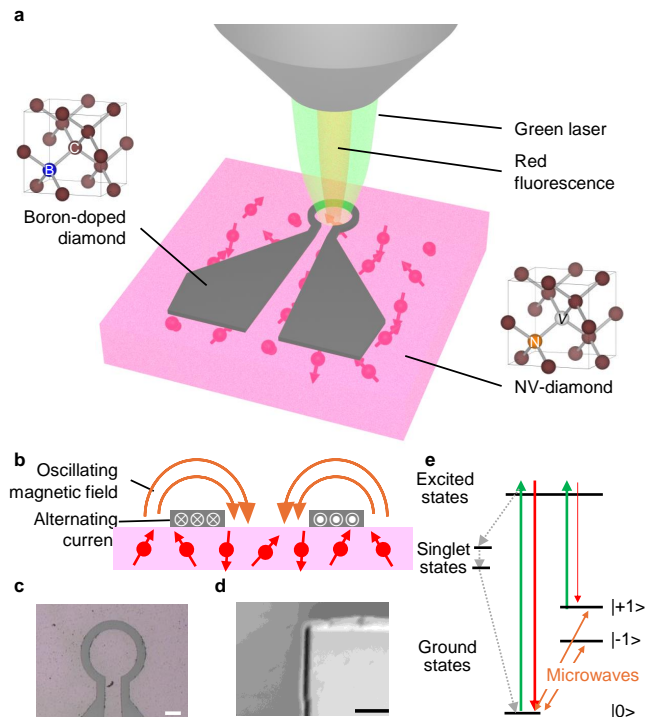


FIG. 1. (Color online) (a) Overview of BDD–NV system, which consists of a Ω -shaped BDD circuit fabricated on a diamond substrate containing an ensemble of NV centers. In this study, we observed NV centers mainly inside the Ω area. Crystal structure of BDD is shown in the left side. C and B denote carbon and boron atoms, respectively. Structure of NV center in diamond lattice is shown in the right side. N and V denote nitrogen atom and vacancy, respectively. (b) Side view of BDD–NV system. A BDD thin film is grown on a single-crystalline diamond, which contains NV centers. The Ω -shaped BDD circuit hosts an alternating current at the microwave frequency range, generating an oscillating magnetic field. This microwave field is used for manipulating the NV centers in the diamond substrate. (c) Optical image of BDD circuit with boron concentration of $3 \times 10^{21} \text{ cm}^{-3}$. Scale bar is $50 \mu\text{m}$. (d) Scanning electron microscope image of edge of BDD thin film grown on single-crystalline diamond substrate with NV centers. Scale bar is $10 \mu\text{m}$. (e) Energy diagram of NV center. The ground states can be excited optically by a 532 nm laser and decay along with spin-dependent fluorescence. The spin state is manipulated by a microwave magnetic field applied by a BDD circuit.

BDD2, and BDD3, corresponding to decreasing boron concentrations from metal to insulator, as detailed in Table I. The BDD circuits were produced in an Ω configuration with an inner diameter of $140 \mu\text{m}$ and thickness of 700 nm via microwave plasma chemical vapor deposition. The boron concentrations were determined via an analysis of the temperature dependence of resistivity, which will be discussed in further detail later.

The diamond substrate measures $3 \text{ mm} \times 3 \text{ mm} \times 0.5 \text{ mm}$ and features a concentration of NV centers at

4.5 ppm across all four crystallographic axes. The NV center possesses an electronic ground-state triplet characterized by the states $|0\rangle$ and $|\pm 1\rangle$, with a separation of 2.87 GHz resulting from spin–spin interactions. Additionally, the $|\pm 1\rangle$ states experience further splitting due to the Zeeman effect when subjected to a finite magnetic field B aligned with the NV axis of interest. The energy levels corresponding to these spin states can be analyzed through optically detected magnetic resonance (ODMR) spectroscopy, which involves observing changes in the red fluorescence of the NV center as the microwave field frequency matches the energy difference between the $|0\rangle$ state and either of the $|\pm 1\rangle$ states [40, 41].

The Ω -shaped BDD circuit operates with alternating current, generating an oscillating magnetic field that ranges from direct current to microwave frequencies. It connects to electrodes on a printed circuit board via a $\phi = 25 \mu\text{m}$ gold wire and silver paste. The printed circuit board is linked to a signal generator through a SubMiniature version A cable, ensuring a matched impedance of 50Ω . The microwave field produced by this BDD circuit enables the manipulation of the ground states of the NV centers, with this study concentrating on the NV centers situated within the Ω -shaped area.

TABLE I. Parameters of BDD circuits. ρ and R. T. denote resistivity and room temperature, respectively. Boron (B) concentration is estimated based on the temperature dependence of resistivity.

	BDD1	BDD2	BDD3
ρ ($\Omega \text{ cm}$) at R. T.	9.8×10^{-4}	4.1×10^{-3}	5.8×10^{-1}
B concentration (cm^{-3})	3×10^{21}	4×10^{20}	1×10^{20}
Thickness (nm)	780	640	690
Conducting state	Metal	Metal	Insulator

III. EVALUATION OF ELECTRICAL PROPERTIES OF BDD

To evaluate the boron concentration of BDD, we first performed electrical resistivity measurements on the BDD circuits, as illustrated in Fig. 2. The electrical resistivity was assessed as a function of temperature using the four-probe technique enclosed in the Physical Properties Measurement System or a home-built Gifford–McMahon cryostat system. BDD1 exhibited metallic characteristics near room temperature, with resistivity decreasing as the temperature decreased. This trend aligns with findings from past studies [1, 4]. Notably, at approximately 3 K , BDD1 displayed a resistivity drop indicative of a superconducting transition. BDD2 showed a similar pattern but without any superconducting transition above 2 K . By contrast, BDD3, with reduced boron concentration, displayed typical insulating behavior, characterized by an increase in resistivity with decreasing temperature. Earlier studies have identified an insulator-

to-metal transition at a boron concentration of approximately $3 \times 10^{20} \text{ cm}^{-1}$ [3, 4]. Based on past studies [4, 42, 43], the boron concentrations were estimated to be 3×10^{21} , 4×10^{20} , and $1 \times 10^{20} \text{ cm}^{-1}$, respectively, categorizing BDD1 and BDD2 as metals and BDD3 as an insulator.

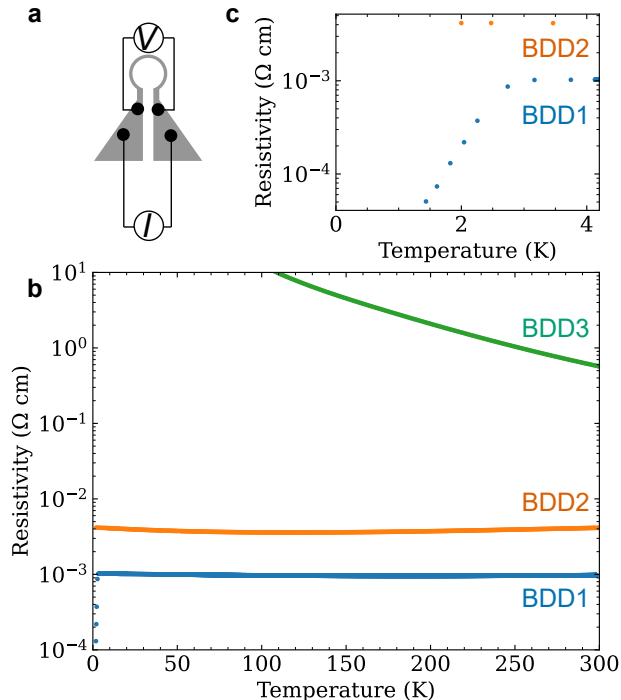


FIG. 2. (Color online) Temperature dependence of electrical resistivity. (a) Four-terminal arrangement used for the measurement method. (b) Temperature dependence of electrical resistivity of BDD for three different boron concentrations. The BDDs have resistivities of 9.8×10^{-4} , 4.1×10^{-3} , and $5.8 \times 10^{-1} \text{ } \Omega \text{ cm}$ at room temperature, respectively. BDD1 and BDD2 show metallic behaviors, while BDD3 shows an insulating behavior. (c) A drop in the resistivity of BDD1 indicates a superconducting transition.

We subsequently assessed the impedance of the BDD circuits across a frequency range of 40 Hz to 1 GHz. The frequency-dependent variations in impedance amplitude and phase for BDDs, illustrated in Fig. 3, were recorded from 40 Hz to 110 MHz and from 1 MHz to 1 GHz using distinct equipment (refer to the methods section for specifics). Consequently, the data points between 1 MHz and 110 MHz exhibit overlap. Impedance measurements were conducted using a coaxial probe that made direct contact with the BDD circuit, with each data point representing the average of five measurements. It was observed that both the amplitude and phase of impedance decline in the high-frequency range, with the onset of this decrease being contingent upon the resistivity of the BDD circuits.

This phenomenon suggests a straightforward lumped parameter circuit model consisting of a parallel resistance

and capacitance, as illustrated in the inset of Fig. 3b. This lumped parameter circuit model has a valid design because the $\sim 200 \text{ } \mu\text{m}$ dimension of the BDD circuit is significantly smaller than the $\sim 10 \text{ cm}$ wavelength of 3 GHz microwave fields. The parasitic capacitance component C is connected in parallel to the resistance component R of the BDD circuit, as depicted in the inset of Fig. 3b, enabling the frequency f dependence of the impedance Z and the phase θ to be expressed as $Z(f) = (1/R + 2j\pi fC)^{-1}$ and $\theta(f) = \tan^{-1}(2\pi fRC)$, respectively, which behaves as a high-pass filter. The measured data fit well with the proposed model, with the fitted values being $R = (3.550 \pm 0.005) \times 10^2 \text{ } \Omega$ and $C = 1.93 \pm 0.01 \text{ pF}$ for BDD1; $R = (1.551 \pm 0.002) \times 10^3 \text{ } \Omega$ and $C = 1.782 \pm 0.008 \text{ pF}$ for BDD2; and $R = (1.6680 \pm 0.0005) \times 10^5 \text{ } \Omega$ and $C = 1.854 \pm 0.002 \text{ pF}$ for BDD3. In particular, the obtained R values are largely consistent with those obtained from resistivity measurements using the four-probe method ($2.819 \times 10^2 \text{ } \Omega$ for BDD1, $1.197 \times 10^3 \text{ } \Omega$ for BDD2, and $1.639 \times 10^5 \text{ } \Omega$ for BDD3). It is anticipated that C will vary with the circuit thickness, which correlates with the electrode size, given that the length and width of the circuit are approximately equal. Notably, the fitted value of C increased with greater circuit thickness.

IV. MANIPULATION OF NV CENTER USING BDD CIRCUITS

The results from the impedance measurements facilitated the development of a microwave circuit designed for driving NV centers. This circuit features a diamond substrate housing an NV spin ensemble, along with an Ω -shaped BDD configuration. The measurements were conducted using an electric circuit system that did not incorporate impedance matching. Allowing the mismatched impedance will facilitate the design of a variety of applications, including integration and operation in extreme environments. The impedance of BDD1 was estimated to be $28.6 \text{ } \Omega$ at a frequency of 2.87 GHz, allowing microwave signals to traverse the circuit. Meanwhile, C exhibited an impedance of $28.7 \text{ } \Omega$ at 2.87 GHz, with R of BDD1 measured at $355 \text{ } \Omega$, and these components are arranged in parallel. It is anticipated that certain microwave signals will propagate through resistance component of the circuit, subsequently irradiating the NV spin ensemble without the need for impedance matching. Furthermore, the impedance measurements indicate that the power of the irradiated microwaves is influenced by the resistance, which correlates with boron concentration.

Through the use of the aforementioned BDD circuits, continuous-wave (CW) ODMR was successfully performed under continuous laser excitation, microwave irradiation, and fluorescence detection. The CW ODMR spectra, presented in Fig. 4, were obtained near the centers of the three Ω -shaped BDD circuits. The microwave input power to the BDD circuits was set to 46.5 dBm,

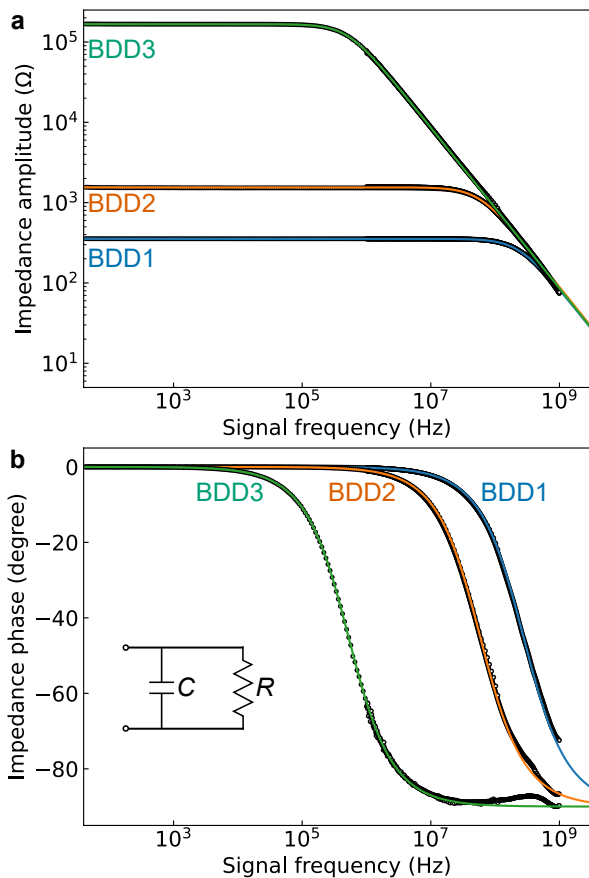


FIG. 3. (Color online) Frequency dependence of impedance (a) amplitude and (b) phase on BDDs. Each data point was obtained using a coaxial probe directly touching the BDD circuits. Note that the values from 40 Hz to 110 MHz and 1 MHz to 1 GHz were obtained using different measurements (refer to the methods section for specifics). Each measurement was repeated 5 times, and their average values were used to minimize the slight differences between different samples. Solid lines represent fitted curves based on model of parallel resistance and capacitance, as shown in inset of (b). Fitted values obtained by fitting the phase are $R = (3.550 \pm 0.005) \times 10^2 \Omega$ and $C = 1.93 \pm 0.01$ pF for BDD1; $R = (1.551 \pm 0.002) \times 10^3 \Omega$ and $C = 1.782 \pm 0.008$ pF for BDD2; and $R = (1.6680 \pm 0.0005) \times 10^5 \Omega$ and $C = 1.854 \pm 0.002$ pF for BDD3, respectively. All error values reported in this paper are estimated based on 1.96σ of parameter fitting, where σ is the standard deviation.

while the laser power directed at the NV-diamond was held constant at 0.33 mW. A static magnetic field of approximately 4.5 mT was applied along the [100] orientation of the NV center using a neodymium permanent magnet. The resulting CW ODMR spectrum displayed resonance dips across all BDDs, including the insulating one. The measured contrasts and full width at half maximum for the resonance between $|0\rangle$ and $|-1\rangle$ at approximately 2.74 GHz were $(0.8 \pm 0.2)\%$ and 4 ± 1 MHz for BDD1, $(0.9 \pm 0.1)\%$ and 4 ± 1 MHz for BDD2, and $(0.20 \pm 0.09)\%$ and 2 ± 1 MHz for BDD3, respectively.

BDD1 and BDD2 exhibited nearly identical contrast and full width at half maximum values, whereas BDD3 exhibited lower contrast, which was attributed to its higher resistivity. Additionally, most of the input microwaves in the GHz range were transmitted through the parasitic capacitance in parallel, leading to small microwave irradiation from the circuit.

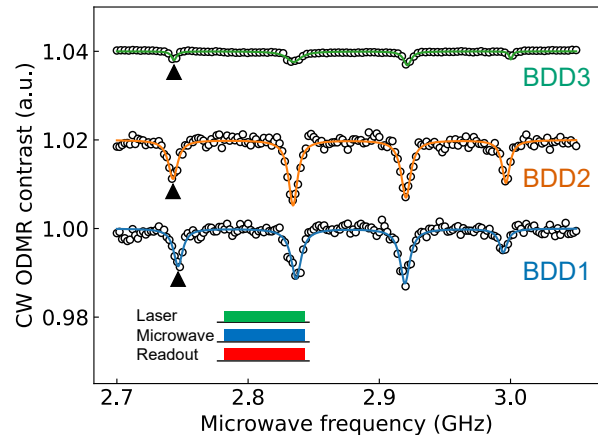


FIG. 4. (Color online) ODMR spectra using different BDDs and their measurement sequences. The signals were obtained from the center of each Ω -shaped circuit. Each spectrum is normalized by its respective maximum intensity and has offset of 0.02 for BDD2, and 0.04 for BDD3. The reconstructed magnetic fields along one NV axis were 4.42 ± 0.03 mT, 4.53 ± 0.02 mT, and 4.68 ± 0.02 mT, respectively. Triangles indicate the frequencies where we conducted pulsed ODMR measurements to observe Rabi oscillations. At each triangle peak, the contrast is $(0.8 \pm 0.2)\%$, $(0.9 \pm 0.1)\%$, and $(0.20 \pm 0.09)\%$ for BDD1, BDD2, and BDD3, respectively. FWHMs are 4 ± 1 MHz, 4 ± 1 MHz, and 2 ± 1 MHz, respectively.

To assess the intensity of microwaves applied to the NV centers, Rabi oscillation measurements were conducted. The measurement protocol involved an initialization laser pulse, a microwave pulse lasting τ , and a readout laser pulse, as illustrated in the inset of Fig. 5. The microwave input power was set to 46.5 dBm, while the laser power was maintained at 0.33 mW. The microwave frequency was adjusted to the frequency of transition between the $|0\rangle$ and $|-1\rangle$ states. Rabi oscillations were successfully recorded for metallic BDD1 and BDD2, as depicted in Fig. 5. The fitted Rabi frequencies were determined to be 6.62 ± 0.04 MHz for BDD1 and 4.19 ± 0.06 MHz for BDD2, indicating that BDD1 exhibited a higher Rabi frequency than that exhibited by BDD2, which implies a variation in the microwave radiation amplitudes. This relation is consistent with what is suggested by the impedance measurements, that the amplitude of the microwaves is influenced by boron concentration. On the other hand, because of its higher resistivity, Rabi oscillations were not detected in BDD3 under the given experimental conditions.

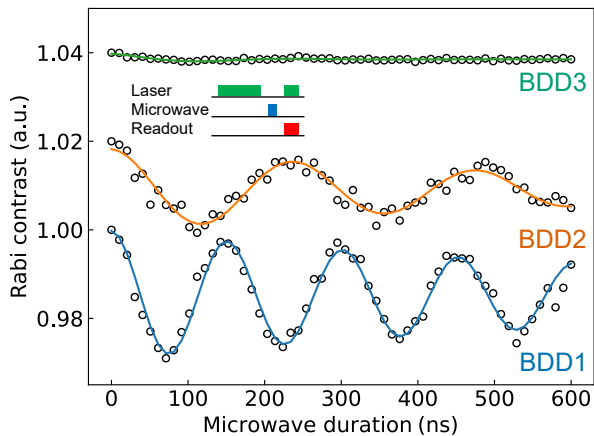


FIG. 5. (Color online) Rabi oscillation using each BDD circuit and its pulse sequence (inset). Rabi contrasts were obtained by dividing the signal by reference measurements at each τ and were offset by 0.02 for BDD2, and 0.04 for BDD3. Each signal was taken at the center of each Ω -shaped circuit. Solid lines indicate the fitted curve. Fitted Rabi frequencies were 6.62 ± 0.04 MHz and 4.19 ± 0.06 MHz, respectively. Signal contrasts are $(2.9 \pm 0.3)\%$ and $(1.8 \pm 0.2)\%$. Decay constants that make amplitudes are $(9 \pm 3) \times 10^2$ ns and $(7 \pm 2) \times 10^2$ ns, respectively.

Mapping the Rabi frequency yields critical insights into the uniformity of the microwave fields, prompting us to conduct Rabi oscillation measurements within the Ω -shaped region. Figure 6a illustrates the spatial variation of the Rabi frequency on BDD1, with the interior of the circuit segmented into a 10×10 pixel grid. Rabi oscillations were recorded at each pixel while constant laser and microwave power levels of 0.33 mW and 46.5 dBm, respectively, were maintained. The oscillations were detected throughout the Ω -shaped loop, revealing a minimum Rabi frequency at the center with an increase toward the periphery. Simulation results are presented in Fig. 6b, demonstrating that the experimental findings align closely with the simulations.

V. DISCUSSION

Enhancing microwave transmission to the BDD circuit, achievable through impedance matching, could enable the driving of NV centers with reduced power consumption or at the increased Rabi frequency. Our impedance measurements reveal that the BDD circuit is characterized by a parallel arrangement of parasitic capacitance C and electrical resistance R . Given that both capacitance and electrical resistance are influenced by the dimensions and structure of the circuit, appropriate geometric adjustments can optimize impedance matching. Additionally, minimizing the resistivity of the BDD is crucial, because improved current propagation on the R channel leads to more efficient generation of the oscillating mag-

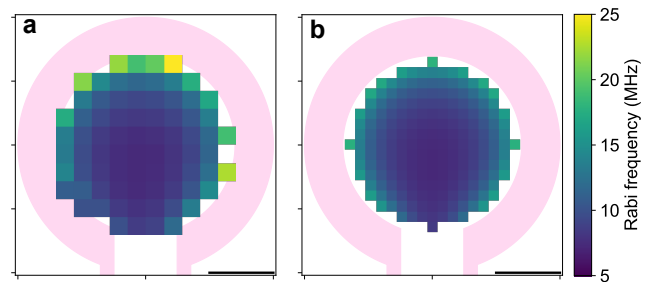


FIG. 6. (Color online) (a) Measured and (b) simulated Rabi frequencies inside Ω -shaped area. Scale bar is $50 \mu\text{m}$. Vacant grid indicates that we did not obtain observable Rabi oscillations, mainly because of intransparency of BDD1 circuit, which prohibited gathering NV fluorescence across the BDD layer. Higher Rabi frequencies are observed at edge of Ω shape but are strongly spatially dependent, meaning that for a single NV center driving where spatial uniformity is not needed, one can use edge of Ω shape.

netic field. Prior research has demonstrated that boron concentration can be elevated to $1 \times 10^{22} \text{cm}^{-3}$ [44], resulting in a corresponding increase in hall concentration to approximately $1 \times 10^{22} \text{cm}^{-3}$, thereby allowing for a further reduction in the resistivity of the BDD utilized in this study.

The benefits of employing a BDD circuit include its robust physical and chemical stability and its capacity for integration. BDD exhibits chemical stability in both acidic and alkaline environments, making it suitable for electrochemical analyses [45, 46]. It can operate effectively under high temperatures and pressures and remains reusable after returning to ambient conditions until it ultimately fails [47–49]. Furthermore, BDD circuits can be patterned precisely at the micrometer scale through microfabrication methods and can be stacked by depositing insulating undoped diamond between them. This enables the development of compact and resilient quantum sensors that integrate NV centers with BDDs, presenting a promising avenue for quantum sensing in challenging environments such as oceans, industrial settings, and outer space [50].

Our electrical measurements suggest that BDD circuits are also effective for generating oscillating electromagnetic fields at lower frequencies, applicable in various domains. For instance, an alternating current at a kilohertz frequency is utilized in the phase-encoding technique, where the orientation of the magnetic field is aligned with its sequence [38, 39], while megahertz radio frequency waves manipulate different nuclear spins both within and outside diamond [35–37, 51]. Given the commendable thermal conductivity of BDD [52], it is anticipated that the heat produced by these alternating currents can be efficiently dissipated at ambient temperatures. The extensive range of operational frequencies further enhances the appeal of BDD circuits, indicating promising prospects in quantum sensing and quantum information processing.

VI. METHOD

A. BDD circuit fabrication

A [100]-oriented single-crystalline diamond substrate purchased from Element Six (DNV-B14) was used in this study. The diamond substrate had a size of $3\text{ mm} \times 3\text{ mm} \times 0.5\text{ mm}$ and contained an ensemble of NV centers with a concentration of 4.5 ppm. BDD was deposited on the diamond substrate using microwave plasma chemical vapor deposition, the procedure of which is described elsewhere [2]. The BDD circuits were fabricated via the following steps: (1) The Ti/Au metal mask was fabricated via lithography and lift-off techniques. (2) The diamond substrate with the metal mask was annealed under vacuum. (3) BDD was selectively deposited on the uncovered region of diamond substrate by microwave plasma chemical vapor deposition. (4) After the deposition, the metal mask was removed via mixed acid treatment. We repeated this process three times to prepare three Ω -shaped BDDs with different boron concentrations on the same diamond substrate. The boron concentration was controlled by changing the ratio of flow rate in methane as a carbon source and trimethylboron as boron source. The inner and outer diameters were $140\ \mu\text{m}$ and $200\ \mu\text{m}$, respectively. All BDDs were of the same shape. Here, we labeled them BDD1, BDD2, and BDD3 in order of decreasing boron concentration.

B. Evaluation of thin film

The thickness of the BDD thin film was measured using an atomic force microscope (Nanocute, SII NanoTechnology Inc.) at room temperature. Scanning electron microscope images were obtained using JSM-6010LA, JEOL with acceleration voltage of 5 keV.

C. Resistivity measurement protocol

The temperature dependence of electrical transport was measured using the current-driven four-probe method with a home-built GM cryostat system for BDD1 and Physical Properties Measurement System (Quantum Design) for BDD2 and BDD3. In the home-built GM cryostat system, an ADCMT 6146 current source and a KEITHLEY 2000 voltage meter were used for the measurements. First, we decreased the temperature from 300 K to 4.2 K, then decreased the chamber pressure using scroll-type-vacuum-pump to reach temperatures below 2 K.

D. Impedance measurement protocol

The frequency dependence of the impedance was measured using two impedance analyzers (4294A and

E4991A, Agilent) at room temperature. We used 4294A for 40 Hz to 110 MHz and E4991A for 1 MHz to 1 GHz. The coaxial probe (CPHF-R-0.5, Yokowo DS) connected to the impedance analyzer was directly put in contact with the BDD circuits to measure the impedance. Each measurement was repeated 5 times, and their average values were used to minimize the slight differences between different samples.

E. ODMR setup

CW ODMR and Rabi oscillation measurements were performed using a home-built confocal microscope. A 0.33 mW, 532 nm green laser beam was generated using a solid-state laser (MGL-III-532-200mW, CNI Laser). The emitted beam was switched using an acousto-optic modulator (AOM, AOMO 3200-121, Gooch&Housego) and irradiated the diamond through a 0.95 NA air objective lens (EC Epiplan-Apochromat 100x/0.95 HD DIC M27, Zeiss). The emitted fluorescence was collected using the same objective lens and detected by a single-photon counting module (SPCM-780-33-BR1, Excelitas). A data acquisition device (NI 6363 and NI PXIe-1073, National Instruments) was used for fluorescence counting. A vector signal generator (SMW 200A, Rohde & Schwarz) output microwave signals for CW measurements, whereas an arbitrary waveform generator (AWG70002A, Tektronix) generated signals for pulsed measurements. These microwave signals selectively passed through a switch (ZASWA-2-50DR+, Mini-Circuit) and were amplified using an amplifier (ZHL-16W-43-S+, Mini-Circuit). For pulsed measurements, a field programmable gate array is used to gate the AOM switch and the microwave source. The amplified microwave signal went through a $50\ \Omega$ PCB and reached the BDD circuits via a $\phi = 25\ \mu\text{m}$ gold wire fixed using Ag paste (4922N, DuPont).

F. Numerical simulation

The mapping of the Rabi frequency f_R was calculated based on $f_R = \sqrt{2}\gamma_e B_z$, where γ_e and B_z denote the gyromagnetic ratio and amplitude of the oscillating field perpendicular to the plane, respectively. The amplitude of the oscillating field was estimated using Biot-Savart's law for a magnetic field generated by an arc with inner and outer diameters of $140\ \mu\text{m}$ and $200\ \mu\text{m}$ and circumscribing angle of 0.77π radian.

ACKNOWLEDGMENTS

The authors would like to thank H. Sano for helping with impedance measurements. This work is supported by, or in part by, JSPS KAKENHI Grant numbers

JP21K14524 and JP23K26528, JSPS Fostering Joint International Research Grant number JP23KK0267, JSPS Bilateral Program Grant number JPJSBP120238803, the National Research Foundation (NRF) of Korea program under Grant No. 2N77160, and KIST institutional program (Project. No. 2E32941). M.O. receives funding from JSPS Grant-in-Aid for JSPS Fellows Grant number JP24KJ1035.

AUTHOR CONTRIBUTIONS

M.O., R.M., and K.A. designed the study. M.O., E.K., R.M. S.O., S.T., H.L., and E.L. conducted electrical, op-

tical, AFM, and SEM measurements, analyzed data, and conducted numerical simulations. R.M. fabricated the BDD device. J.L., Y.T., and K.A. conceived the application of the BDD to ODMR and supervised the project. All authors discussed the results and participated in writing the manuscript. All the authors discussed the results and commented on the manuscript.

COMPETING INTERESTS

The authors have no competing interests to disclose.

-
- [1] E. A. Ekimov, V. A. Sidorov, E. D. Bauer, N. N. Mel'nik, N. J. Curro, J. D. Thompson, and S. M. Stishov, *Nature* **428**, 542 (2004).
- [2] Y. Takano, M. Nagao, I. Sakaguchi, M. Tachiki, T. Hatano, K. Kobayashi, H. Umezawa, and H. Kawarada, *Applied Physics Letters* **85**, 2851 (2004).
- [3] T. Yokoya, T. Nakamura, T. Matsushita, T. Muro, Y. Takano, M. Nagao, T. Takenouchi, H. Kawarada, and T. Oguchi, *Nature* **438**, 647 (2005).
- [4] Y. Takano, *J. Phys.: Condens. Matter* **21**, 253201 (2009).
- [5] S. Mandal, T. Bautze, O. A. Williams, C. Naud, É. Bustarret, F. Omnès, P. Rodière, T. Meunier, C. Bäuerle, and L. Saminadayar, *ACS Nano* **5**, 7144 (2011).
- [6] T. Kageura, M. Hideko, I. Tsuyuzaki, A. Morishita, A. Kawano, Y. Sasama, T. Yamaguchi, Y. Takano, M. Tachiki, S. Ooi, K. Hirata, S. Arisawa, and H. Kawarada, *Sci Rep* **9**, 15214 (2019).
- [7] B. Oripov, D. Kumar, C. Garcia, P. Hemmer, T. Venkatesan, M. S. Ramachandra Rao, and S. M. Anlage, *Applied Physics Letters* **118**, 242601 (2021).
- [8] J. A. Cuenca, T. Brien, S. Mandal, S. Manifold, S. Doyle, A. Porch, G. M. Klemencic, and O. A. Williams, *Carbon* **201**, 251 (2023).
- [9] J. Isberg, J. Hammersberg, E. Johansson, T. Wikström, D. J. Twitchen, A. J. Whitehead, S. E. Coe, and G. A. Scarsbrook, *Science* **297**, 1670 (2002).
- [10] M. W. Geis, T. C. Wade, C. H. Wuorio, T. H. Fedynyshyn, B. Duncan, M. E. Plaut, J. O. Varghese, S. M. Warnock, S. A. Vitale, and M. A. Hollis, *physica status solidi (a)* **215**, 1800681 (2018).
- [11] N. Donato, N. Rouger, J. Pernot, G. Longobardi, and F. Udrea, *J. Phys. D: Appl. Phys.* **53**, 093001 (2019).
- [12] D. Das, R. Raj, J. Jana, S. Chatterjee, K. L. Ganapathi, M. Chandran, and M. S. R. Rao, *J. Phys. D: Appl. Phys.* **55**, 333002 (2022).
- [13] F. Jelezko, T. Gaebel, I. Popa, A. Gruber, and J. Wrachtrup, *Phys. Rev. Lett.* **92**, 076401 (2004).
- [14] T. Gaebel, M. Domhan, I. Popa, C. Wittmann, P. Neumann, F. Jelezko, J. R. Rabeau, N. Stavrias, A. D. Greentree, S. Praver, J. Meijer, J. Twamley, P. R. Hemmer, and J. Wrachtrup, *Nature Phys* **2**, 408 (2006).
- [15] F. Jelezko, T. Gaebel, I. Popa, M. Domhan, A. Gruber, and J. Wrachtrup, *Phys. Rev. Lett.* **93**, 130501 (2004).
- [16] R. Hanson, F. M. Mendoza, R. J. Epstein, and D. D. Awschalom, *Phys. Rev. Lett.* **97**, 087601 (2006).
- [17] M. V. G. Dutt, L. Childress, L. Jiang, E. Togan, J. Maze, F. Jelezko, A. S. Zibrov, P. R. Hemmer, and M. D. Lukin, *Science* **316**, 1312 (2007).
- [18] J. M. Taylor, P. Cappellaro, L. Childress, L. Jiang, D. Budker, P. R. Hemmer, A. Yacoby, R. Walsworth, and M. D. Lukin, *Nature Phys* **4**, 810 (2008).
- [19] C. L. Degen, *Applied Physics Letters* **92**, 243111 (2008).
- [20] G. Balasubramanian, I. Y. Chan, R. Kolesov, M. Al-Hmoud, J. Tisler, C. Shin, C. Kim, A. Wojcik, P. R. Hemmer, A. Krueger, T. Hanke, A. Leitenstorfer, R. Bratschitsch, F. Jelezko, and J. Wrachtrup, *Nature* **455**, 648 (2008).
- [21] J. R. Maze, P. L. Stanwix, J. S. Hodges, S. Hong, J. M. Taylor, P. Cappellaro, L. Jiang, M. V. G. Dutt, E. Togan, A. S. Zibrov, A. Yacoby, R. L. Walsworth, and M. D. Lukin, *Nature* **455**, 644 (2008).
- [22] V. M. Acosta, E. Bauch, M. P. Ledbetter, C. Santori, K.-M. C. Fu, P. E. Barclay, R. G. Beausoleil, H. Linget, J. F. Roch, F. Treussart, S. Chemerisov, W. Gawlik, and D. Budker, *Phys. Rev. B* **80**, 115202 (2009).
- [23] E. Schaefer-Nolte, F. Reinhard, M. Ternes, J. Wrachtrup, and K. Kern, *Review of Scientific Instruments* **85**, 013701 (2014).
- [24] P. Bhattacharyya, W. Chen, X. Huang, S. Chatterjee, B. Huang, B. Kobrin, Y. Lyu, T. J. Smart, M. Block, E. Wang, Z. Wang, W. Wu, S. Hsieh, H. Ma, S. Mandyam, B. Chen, E. Davis, Z. M. Geballe, C. Zu, V. Struzhkin, R. Jeanloz, J. E. Moore, T. Cui, G. Galli, B. I. Halperin, C. R. Laumann, and N. Y. Yao, *Nature* **627**, 73 (2024).
- [25] M. Wang, Y. Wang, Z. Liu, G. Xu, B. Yang, P. Yu, H. Sun, X. Ye, J. Zhou, A. F. Goncharov, Y. Wang, and J. Du, *Nat Commun* **15**, 8843 (2024).
- [26] P. J. Scheidegger, S. Diesch, M. L. Palm, and C. L. Degen, *Applied Physics Letters* **120**, 224001 (2022).
- [27] G.-Q. Liu, X. Feng, N. Wang, Q. Li, and R.-B. Liu, *Nat Commun* **10**, 1344 (2019).
- [28] K. Kubota, Y. Hatano, Y. Kainuma, J. Shin, D. Nishitani, C. Shinei, T. Taniguchi, T. Teraji, S. Onoda, T. Ohshima, T. Iwasaki, and M. Hatano, *Diamond and Related Materials* **135**, 109853 (2023).

- [29] J.-W. Fan, S.-W. Guo, C. Lin, N. Wang, G.-Q. Liu, Q. Li, and R.-B. Liu, *Nano Lett.* **24**, 14806 (2024).
- [30] D. Kim, M. I. Ibrahim, C. Foy, M. E. Trusheim, R. Han, and D. R. Englund, *Nat Electron* **2**, 284 (2019).
- [31] F. M. Stürner, A. Brenneis, T. Buck, J. Kassel, R. Rölver, T. Fuchs, A. Savitsky, D. Suter, J. Grimmel, S. Hengesbach, M. Förtsch, K. Nakamura, H. Sumiya, S. Onoda, J. Isoya, and F. Jelezko, *Advanced Quantum Technologies* **4**, 2000111 (2021).
- [32] K. Omirzakhov, M. H. Idjadi, T.-Y. Huang, S. A. Breitwieser, D. A. Hopper, L. C. Bassett, and F. Aflatouni, *IEEE Transactions on Microwave Theory and Techniques* **71**, 4052 (2023).
- [33] H. Kumar, S. Dasika, M. Mangat, S. Tallur, and K. Saha, *Review of Scientific Instruments* **95**, 075002 (2024).
- [34] M. W. Doherty, N. B. Manson, P. Delaney, F. Jelezko, J. Wrachtrup, and L. C. L. Hollenberg, *Physics Reports The Nitrogen-Vacancy Colour Centre in Diamond*, **528**, 1 (2013).
- [35] L. Jiang, J. S. Hodges, J. R. Maze, P. Maurer, J. M. Taylor, D. G. Cory, P. R. Hemmer, R. L. Walsworth, A. Yacoby, A. S. Zibrov, and M. D. Lukin, *Science* **326**, 267 (2009).
- [36] P. Neumann, J. Beck, M. Steiner, F. Rempp, H. Fedder, P. R. Hemmer, J. Wrachtrup, and F. Jelezko, *Science* **329**, 542 (2010).
- [37] I. Lovchinsky, A. O. Sushkov, E. Urbach, N. P. de Leon, S. Choi, K. De Greve, R. Evans, R. Gertner, E. Bersin, C. Müller, L. McGuinness, F. Jelezko, R. L. Walsworth, H. Park, and M. D. Lukin, *Science* **351**, 836 (2016).
- [38] K. Arai, C. Belthangady, H. Zhang, N. Bar-Gill, S. J. DeVience, P. Cappellaro, A. Yacoby, and R. L. Walsworth, *Nature Nanotech* **10**, 859 (2015).
- [39] G. Zhang, Y. Liu, J. J. Raftery, and A. A. Houck, *npj Quantum Inf* **3**, 1 (2017).
- [40] E. van Oort, N. B. Manson, and M. Glasbeek, *J. Phys. C: Solid State Phys.* **21**, 4385 (1988).
- [41] A. Gruber, A. Dräbenstedt, C. Tietz, L. Fleury, J. Wrachtrup, and C. von Borczyskowski, *Science* **276**, 2012 (1997).
- [42] R. J. Zhang, S. T. Lee, and Y. W. Lam, *Diamond and Related Materials* **5**, 1288 (1996).
- [43] J. P. Lagrange, A. Deneuve, and E. Gheeraert, *Diamond and Related Materials* **7**, 1390 (1998).
- [44] A. Kawano, H. Ishiwata, S. Iriyama, R. Okada, T. Yamaguchi, Y. Takano, and H. Kawarada, *Phys. Rev. B* **82**, 085318 (2010).
- [45] T. Yano, D. A. Tryk, K. Hashimoto, and A. Fujishima, *J. Electrochem. Soc.* **145**, 1870 (1998).
- [46] D. Gandini, E. Mahé, P. Michaud, W. Haenni, A. Perret, and Ch. Comminellis, *Journal of Applied Electrochemistry* **30**, 1345 (2000).
- [47] R. Matsumoto, Y. Sasama, M. Fujioka, T. Irifune, M. Tanaka, T. Yamaguchi, H. Takeya, and Y. Takano, *Review of Scientific Instruments* **87**, 076103 (2016).
- [48] R. Matsumoto, M. Einaga, S. Adachi, S. Yamamoto, T. Irifune, K. Terashima, H. Takeya, Y. Nakamoto, K. Shimizu, and Y. Takano, *Supercond. Sci. Technol.* **33**, 124005 (2020).
- [49] R. Matsumoto, K. Yamane, T. Tadano, K. Terashima, T. Shinmei, T. Irifune, and Y. Takano, (2024), arXiv:2409.03409 [cond-mat].
- [50] K.-M. C. Fu, G. Z. Iwata, A. Wickenbrock, and D. Budker, *AVS Quantum Science* **2**, 044702 (2020).
- [51] F. Bruckmaier, R. D. Allert, N. R. Neuling, P. Amrein, S. Littin, K. D. Briegel, P. Schätzle, P. Knittel, M. Zaitsev, and D. B. Bucher, *Science Advances* **9**, eadh3484 (2023).
- [52] D. Prikhodko, S. Tarelkin, V. Bormashov, A. Golovanov, M. Kuznetsov, D. Teteruk, N. Kornilov, A. Volkov, and A. Buga, *J. Superhard Mater.* **41**, 24 (2019).